





Fibril growth captured by electrical properties of amyloid- β and human islet amyloid polypeptidePrasoon Awasthi ^{1,*}, Anurag Singh ^{2,*}, Suparna Khatun ², Amar Nath Gupta ² and Soumen Das ^{1,†}¹*BioMEMS Laboratory, School of Medical Science and Technology, Indian Institute of Technology Kharagpur, 721302, India*²*Biophysics and Soft Matter Laboratory, Department of Physics, Indian Institute of Technology Kharagpur, 721302, India*

(Received 15 February 2020; revised manuscript received 12 May 2020; accepted 22 May 2020; published 15 June 2020)

The aggregation of amyloid- β ($A\beta$) and human islet amyloid polypeptide (hIAPP) proteins have attracted considerable attention because of their involvement in protein misfolding diseases. These proteins have mostly been investigated using atomic force microscopy, transmission electron microscopy, and fluorescence microscopy to study the directional growth of fibrils both perpendicular to and along the fibril axis. Here, we demonstrate the real-time monitoring of the directional growth of fibrils in terms of activation energy of proton transfer using an impedance spectroscopy technique. The activation energy is used to quantify the sensitivity of proton conduction to the different stages of protein aggregation. The decrement (increment) in activation energy is related to the fibril growth along (perpendicular to) the fibril axis in intrinsic protein aggregation. The entire aggregation process shows different phases of the directional growth for $A\beta$ and hIAPP, indicating different pathways for their aggregation. The activation energy for hIAPP is found to be smaller than the activation energy of $A\beta$ during the aggregation process. The oscillatory behavior of the activation energy of hIAPP reflects a rapid change in the directional growth of the protofilaments of hIAPP. The results indicate higher aggregation propensity of $A\beta$ than hIAPP. In the presence of resveratrol, hIAPP exhibits slower aggregation compared to $A\beta$. Methods of this study may in general be used to reveal the modulated aggregation pathway of proteins in the presence of different ligands.

DOI: [10.1103/PhysRevE.101.062413](https://doi.org/10.1103/PhysRevE.101.062413)**I. INTRODUCTION**

Proton transport at the molecular level is involved in various biochemical reactions essential for cell regulation. For the first time in 1806, Grotthuss described the proton transport mechanism between water molecules via hydrogen bonding, which facilitates proton mobility [1,2]. Further, proton transport through biomembrane was deciphered by Nagle *et al.*, in which hydrogen bonding between the side chains of different residues of protein such as serine, threonine, and tyrosine was shown to act as a sort of wire for proton transfer [3]. A very similar concept of proton transfer was used to describe different proteins such as ATPase, green fluorescent protein (GFP), cytochrome c oxidase, cytochrome b_6f , and bacteriorhodopsin [4–12].

The hydrogen bonding between the side chains of amino acids is one of the stabilizing features in the aggregates of pathologically relevant proteins, commonly known as amyloids [13,14]. In amyloids, the aggregates are formed in three steps: First the individual protein strands stack to form β -sheets. In the second step, these β -sheets form cross-zipper structures, wherein amide side chains acquire proper rotamers to facilitate the interdigitation of the side chains. In the final step, the interaction between pairs of sheets leads to the formation of fibrils. The interstrand hydrogen bonding between the side chains of polar residues starts appearing during the

formation of β -sheets [13,14]. These hydrogen bonds may act as a proton wire, transferring protons via the process of sequential jumping. As the protein starts aggregating, the passage for proton conduction along the proton wire continuously gets modified.

The changes in the proton conduction are mainly due to elongation of the protofilaments both perpendicular to and along the fibril axis. The crystallographic cross-zipper structures of amyloids have been shown to have an interstrand distance of 4.8 Å and an intersheet separation of 10 Å [15]. This suggests that proton hopping through the hydrogen bonds formed between the side chains of interstrand residues will have less activation energy compared to the intersheet hydrogen bonds. Because of this, the protofilament growth perpendicular to and along the fibril axis will inhibit and favor the proton conduction, respectively. Hence, the pathway of proton conduction and its change may help to monitor the direction (perpendicular to and/or along the fibril axis) of fibril growth. Previously, atomic force microscopy, transmission electron microscopy, and fluorescence microscopy imaging techniques have been used to monitor the directional growth of fibrils of hIAPP and $A\beta$ [16–18]. However, these techniques have limitations in preserving the real-time protein dynamics while imaging the protein samples. In AFM, protein samples deposited on substrate induce a catalytic effect changing the progression of protein aggregation. TEM provides static information as one needs to perform *ex situ* at discrete time, and labeling with fluorophores in fluorescence microscopy alters protein dynamics. Notably, the changes in the proton conduction do not suffer from these limitations and

*These authors contributed equally to this work.

†Corresponding author: sou@smst.iitkgp.ernet.in

are used here to monitor the intrinsic aggregation of $A\beta$ and hIAPP. Herein, the changes in the proton conduction during protein aggregation are quantified by an electrical parameter: the activation energy of proton transfer, calculated from the measured impedance of the protein solutions using impedance spectroscopy (IS).

Recently, using the IS technique, Rafael *et al.* have studied the fibrillation kinetics of human insulin by calculating the resistance and constant phase element of the bulk solution [19]. The inhibition capability of the doxycycline drug was tested for the aggregation of carboxymethylated K-casein milk protein by calculating the capacitance of fibril precipitation on the electrodes [20]. However, the use of the electrical circuits has not been consistent, and interpretation of electrical elements is not unique in IS measurements. In the literature, electrochemical sensing of β -amyloid is also explored for Alzheimer disease (AD) management [21]. Here, we show the real-time monitoring of protein aggregation and inhibition by calculating the activation energy of proton transfer during the process without employing any equivalent electrical circuit. In the present work, two proteinopathy-related proteins, (i) amyloid β ($A\beta$, 1–42 aa) causing AD [17] and (ii) human islet amyloid polypeptide (hIAPP also known as human amylin, 1–37 aa), which is related to type II diabetes mellitus (T2DM) [22], were studied for electrical characterization by IS. The experiments were performed using a miniaturized device under the temperature gradient environment of 5 °C (45–40 °C) at 20 μ M protein concentration. For $A\beta$, the growth along the fibril axis first dominates the aggregation process and then proceeds by the elongation in the direction perpendicular to the fibril axis. In the case of hIAPP, the monomeric states are initially stabilized by repulsive interactions followed by the growth of the protofilaments both perpendicular to and along the fibril axis. Moreover, the inhibition capability of resveratrol (Res) was explored under similar ambient conditions with $A\beta$ and hIAPP mixed with Res in the molar ratio of 1:1 (AB1R1 and A1R1) and 1:5 (AB1R5 and A1R5). The results indicate a modified aggregation pathway for both the proteins and Res shows better inhibition for hIAPP compared to $A\beta$.

II. MATERIALS AND METHODS

A. Sample preparation

Human amyloid- β (1–42 aa, $M_w = 4514.4 \text{ g mol}^{-1}$) and hIAPP (1–37 aa, $M_w = 3904 \text{ g mol}^{-1}$) purchased from the Anaspec Peptide were used to prepare the samples. The stock solutions of proteins were dissolved in dimethyl sulfoxide (DMSO) separately, and later the solutions were diluted in filtered phosphate buffer saline (PBS; 1X) in different aliquots. These samples were sonicated for 1 h and centrifuged for 10 min at 1000 rpm to produce homogeneous solutions. The final concentration of proteins was used at 20 μ M at pH 6.5 ± 0.1 . Further, resveratrol was added with the protein solutions in a molar ratio of 1:1 and 1:5 to study its effect on the aggregation of the proteins.

B. Device design and data acquisition

Two devices (device 1 and device 2), each having two platinum wire electrodes surrounded by a well on a glass

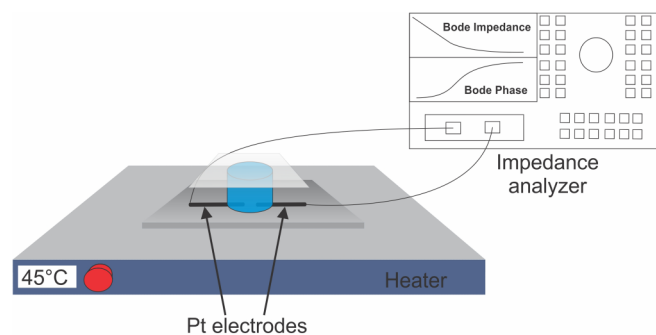


FIG. 1. The schematic diagram of the experimental setup used to obtain the impedance spectra of protein solutions and buffer.

substrate, were designed for measuring the impedance of the buffer, $A\beta$ (1–42), hIAPP (1–37), and the samples prepared by proteins mixed with resveratrol molecules. In each device, electrodes having a 3-mm gap were fixed on a glass substrate by making a circular boundary of polydimethyl siloxane (PDMS, Sylgard 184, Dow Corning, USA) prepolymer in the ratio of 10:1 (monomer to curing agent), which was cured at 120 °C for 5 min. Further, on the top of this boundary, a well of 450 μ l in volume was attached similarly using PDMS. Impedance data of all the solutions were recorded four to five times using an impedance analyzer (Agilent 4294A) at 20 mV RMS from 73 to 869 kHz frequency range at 5 ± 0.3 °C (45.8 ± 0.5 to 40.8 ± 0.7 °C) temperature gradient for 350 min at 5-min intervals. The temperature gradient was confirmed by using a thermal imager, Fluke Ti32. Figure 1 depicts the schematic of the experimental setup consisting of the device on the hot plate at 45 °C connected with the impedance analyzer for measuring the impedance of the solutions.

C. Statistical analysis

Three different regions were identified for performing the unpaired two-tail Student's *t*-test between the groups $A\beta$ -AB1R1, $A\beta$ -AB1R5, hIAPP-A1R1, and hIAPP-A1R5. The regions A, B, and C span 15–30, 180–195, and 320–335 min respectively. Statistical significance was denoted as * $p < 0.05$, ** $p < 0.01$, *** $p < 0.001$, and NS (not significant), and the calculated *p* values are also displayed in the graphs.

D. Fourier-transform infrared spectroscopy (FTIR) analysis

The protein samples were drop-casted on KBr pellet, and the FTIR spectra (Nicolet 6700, Thermo Fisher) were recorded on the dried samples in the wave-number range 400–4000 cm^{-1} . To resolve the peaks in the FTIR spectra, its second derivative was taken. The second derivative spectra were then multifitted with Gaussian functions to estimate position, width, height, and percentage of secondary structures in the amide I region (1600–1700 cm^{-1}); the percentage was determined as a fraction of total area under this spectral range. Location of the peak (mean), width (FWHM), and height of the peak were the free parameters during the fitting, and χ^2 was chosen as the goodness-of-fit parameter for the convergence of fit (see the Supplemental Material [23]).

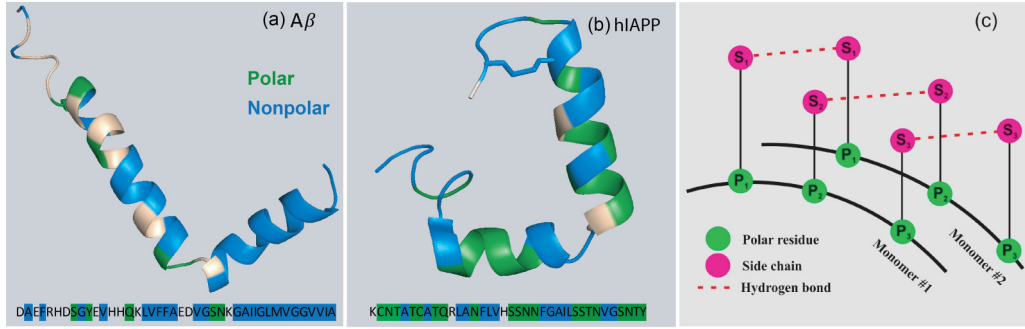


FIG. 2. The protein sequences of the crystallized (a) Aβ (1–42), (b) hIAPP (1–37) taken from RCSB having the PDB IDs 1YLT (Aβ), and 2L86 (hIAPP) respectively, and (c) schematic diagram of the hydrogen bonds between the two side chains; green and magenta colors show the polar residues and its corresponding side chains present in monomers respectively, whereas the red dotted line represents the hydrogen bonding between the side chains.

III. THEORY AND CALCULATION

The Nernst-Planck equation describes the transport of charged species in the protein solution under an applied potential difference (V) and is given by

$$J_i = -D_i \left[\nabla n_i + \frac{z_i F}{RT} n_i \nabla V \right], \quad (1)$$

where $V = V_0 \sin(\omega t)$, J_i is the flux of the i -type charged species, D_i is ion diffusivity, n_i is the number concentration of ion, z_i is the valence of ion, F is Faraday’s constant, R is the universal gas constant, and T is the absolute temperature. In the buffer media, the proton transfer occurs by the mechanism of proton hopping through the hydrogen bonding between water molecules as described by the Grothuss mechanism [1]. When the protein is dissolved into the buffer, its residues show polar and nonpolar natures, as shown in Fig. 2(a) for Aβ and Fig. 2(b) for hIAPP. The polar residues are primarily contained in the hydrophilic region of the protein, which interacts with the solvent. The proton hopping will be mediated by the side chains of the polar residues present in the protein monomers, as shown in Fig. 2(c), which reflects in the activation energy of the proton conduction. Here, the activation energy for proton transfer (E_P) through the hydrogen bonds between the side chains of polar residues is obtained by subtracting the activation energy of electrical conductivity for protein solution (E_{PS}) to buffer solution (E_B).

The Arrhenius equation for electrical conductivity describes the relationship between the activation energy of electrical conductivity and dc electrical conductivity of the solution [the estimation of dc electrical conductivity from ac impedance is described using Eq. (8)] as the following equation:

$$\sigma = (\sigma_o/T) \exp(-E_a/RT), \quad (2)$$

where σ_o is the pre-exponential factor and E_a is the activation energy determined from the electrical conductivity of the solution. Further, Eq. (2) is used to obtain the E_P as described below:

$$E_P = E_{PS} - E_B = -RT \ln(1 - X), \quad (3)$$

$$X = (\sigma_B - \sigma_{PS})/\sigma_B, \quad (4)$$

where σ_B and σ_{PS} are the dc electrical conductivities of the buffer and the protein solution, respectively, while having a similar pre-exponential factor. The pre-exponential factor depends on the static dielectric constant of the solution [24], which is the lower frequency region of the relative permittivity of the solution. If the static dielectric constant is identical for the buffer and the protein solution, the pre-exponential factor will also be similar. To investigate this, the relative permittivity (or dielectric constant, ϵ_r) of the buffer and the protein solutions are obtained using the following standard equations:

$$\epsilon_r = \epsilon' + i\epsilon'', \quad (5)$$

$$\epsilon' = C_P/C_o, \quad (6)$$

$$\epsilon'' = 1/(\omega R_P C_o), \quad (7)$$

where ω is the angular frequency, C_P and R_P are the capacitance and resistance of the solution, and C_o is the capacitance of air (without solution). Figure 3 presents the variation of relative permittivity with respect to frequency for all the protein solutions at 10 and 345 min. At lower frequencies, polarized molecules align themselves with subsequent changes in the direction of the ac field and result in storage of energy, as evident from the higher values of the relative permittivity in Fig. 3, whereas when those molecules are not aligned at higher frequencies, they do not store the energy, exhibiting lower relative permittivity values. From the graph, it is observed that relative permittivity in the lower frequency region (or static dielectric constant) for the buffer and the protein solutions are identical, resulting in the same pre-exponential factor. Now to calculate the E_P using Eq. (3), temperature (T) is kept as 315.65 K (average of 45°C and 40°C temperature), and the dc electrical conductivities of buffer and protein solutions are required.

The dc electrical conductivity of the solution is calculated by the following relation:

$$\sigma = k/R_b \quad (8)$$

where σ (S/m) is the dc electrical conductivity of the solution, k (m^{-1}) is the cell constant of the device, and R_b (Ω) is the bulk solution resistance. The R_b for all the samples is obtained by taking the impedance value of the solution where the phase

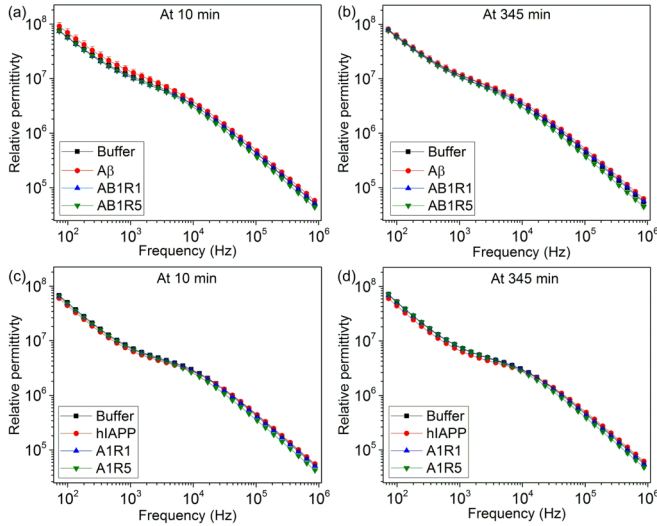


FIG. 3. The relative permittivity of buffer, $A\beta$, AB1R1, and AB1R5 solutions at (a) 10 min and (b) 345 min using device 1; similarly relative permittivity of buffer, hIAPP, A1R1, and A1R5 solutions at (c) 10 min and (d) 345 min using device 2. The graphs display the identical relative permittivity in the lower frequency region (or static dielectric constant) of all the protein solutions, resulting in the similar pre-exponential factor for each solution.

angle is approximately zero (here 868.47 kHz frequency). The cell constant of both devices is obtained by using three different NaCl solutions having concentrations 0.312, 0.625, and 1.25 mg/ml. This parameter is calculated using the equation [25]

$$k = |Z| \sqrt{\sigma_S^2 + \omega^2 \epsilon_0 \epsilon_r} \quad (9)$$

where ϵ_0 is the vacuum permittivity (F/m) and σ_S (S/m), ϵ_r , and Z (Ω) are the electrical conductivity, relative permittivity, and measured impedance of the NaCl solution respectively. The electrical conductivity and relative permittivity of the NaCl solutions are tabulated in Table I. The obtained cell constants of device 1 and device 2 at 868.47 kHz frequency are 707.17 ± 2.41 and $663.76 \pm 4.85 \text{ m}^{-1}$ respectively.

IV. RESULTS AND DISCUSSION

A. Activation energy for proton transfer in $A\beta$ and hIAPP aggregation

The electrical conductivity of buffer, $A\beta$, AB1R1, and AB1R5 solutions using device 1 and buffer, hIAPP, A1R1,

TABLE I. Electrical properties of the solutions used to calculate the cell constant.

NaCl solution concentration (mg/ml)	Approx. conductivity (S/m)	Approx. relative permittivity (ϵ_r) [25]
0.312	0.0764	80.2
0.625	0.1356	80.1
1.250	0.2485	79.8

and A1R5 solutions using device 2 with time are shown in Figs. 4(a) and 4(b), respectively. The process of obtaining dc conductivity by using ac impedance is explained in Sec. III. This process offers an advantage over the dc method by avoiding blocking of ions present in solution [26]. In the case of buffer solution, the electrical conductivity is increasing with time because atmospheric CO_2 gas diffuses through the well and dissolves into the water, leading to the formation of carbonate and bicarbonate ions in the solution [27]. In the case of the protein solution, both the above-mentioned effect and the aggregation could be the reason for the increase in electrical conductivity. However, the CO_2 gas effect cancels out while estimating the activation energy for E_P using Eq. (4).

The electrical conductivities shown in Fig. 4 were used to calculate the activation energy of the protein solutions. Figures 5(a) and 5(b) show the modulus of E_P for $A\beta$ ($E_{P, A\beta}$), and hIAPP ($E_{P, \text{hIAPP}}$), respectively, during the aggregation process. In $A\beta$ aggregation, the hydrophobic interactions, π - π interactions, covalent interactions, and van der Waals interactions between the monomers may result in the formation of dimers [28,29]. The nucleation sites are formed due to these interactions, which further leads to the formation of oligomers. The elongation of nucleation sites dominates along the fibril axis, which leads to the protofilaments formation. The outcome of this elongation process is the increment in the length of the proton wire, which lowers the $E_{P, A\beta}$, as shown in region I of Fig. 5(a), by providing the directional flow of protons due to the tunneling effect. The elongation along the fibril axis is later restricted mainly because of the increased strain in the overtwisted parallel β -sheets, resulting in the breakage of protofilaments into smaller oligomers [30] [transition point between regions I and II in Fig. 5(a)]. Because of this event, the energy barrier for proton conduction starts increasing due to the breakage of long pathways of hydrogen bonds. The oligomers start forming pairs of β -sheets (steric zipper) by removing water, and the side chains of Q15 and N27 polar residues reside inside the hydrophobic core of the structure [17,31]. This event will reduce the total number of sites for proton transfer and will further increase the $E_{P, A\beta}$ [region II in Fig. 5(a)]. The estimated $E_{P, A\beta}$ at the end of the aggregation process is even higher than that of the monomeric state of the protein because the sites responsible for the proton hopping are lesser than the sites present initially in the monomers [region III in Fig. 5(a)].

In the case of hIAPP, monomers are initially stabilized by the repulsive interactions [32] and the intramolecular disulfide bond between C2 and C7 residues [region I in Fig. 5(b)]. The stabilization process delays the aggregation of hIAPP, which is observed as the small fluctuations in $E_{P, \text{hIAPP}}$ [region I in Fig. 5(b)]. Later, the formation of the intermolecular disulfide bond results in the instability of hIAPP structure [33]. This structural instability leads the monomers to form nucleation sites, and the formed oligomers will stack into steric zipper structures. As an outcome of this process, few polar residues at the interface of the two monomers will be in the interior of layers of steric zippers [34]. This will reduce the total number of sites for proton transport, observed as an increase in the $E_{P, \text{hIAPP}}$ [region II in Fig. 5(b)]. Later, the steric zippers further interact to form large oligomers governed by different interactions such as hydrophobic, aromatic interactions,

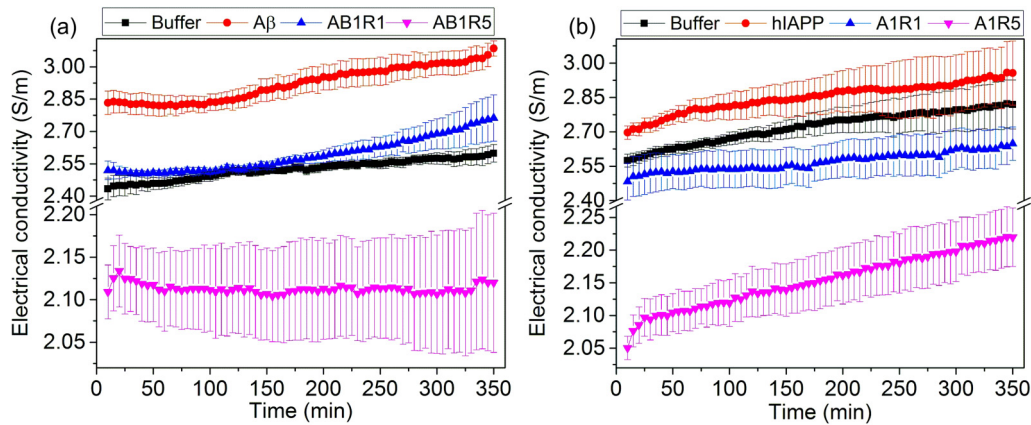


FIG. 4. The electrical conductivity with mean±sd (calculated from four to five independent experiments using fresh samples) of (a) buffer, Aβ, AB1R1, and AB1R5 using device 1 and (b) buffer, hIAPP, A1R1, and A1R5 using device 2 obtained with time.

π - π stacking, short-range attraction, and long-range repulsive interactions [35–37], resulting in the decrement of $E_{P, hIAPP}$ [region III in Fig. 5(b)] due to the increment in the length of the proton wire. The $E_{P, hIAPP}$ at the end of the aggregation is similar to the monomeric state of the protein, which we suspect is due to the significant growth of the protofilaments in

the perpendicular direction. The growth perpendicular to the fibril axis does not contribute to the increment in the length of the proton wire and also reduces the number of hydrogen bonding sites available for the proton conduction.

Comparatively, the $E_{P, hIAPP}$ is less than the $E_{P, A\beta}$ during the entire aggregation period. This is because the number of polar residues participating in the proton transfer process in hIAPP compared to Aβ is higher, indicating more transport of protons through interstrand hydrogen bonds formed between the side chains. Overall, it is observed from the initial (until 120 min) behavior of E_P that Aβ has a higher propensity to aggregate than hIAPP. Moreover, there are profound oscillations in the $E_{P, hIAPP}$ compared to the $E_{P, A\beta}$, indicating more rapid changes in the direction of growth of the protofilaments. Similar oscillations in the shape factor of the aggregates were observed previously where the aggregation of hIAPP was monitored with time using light scattering [32]. In region III, the growth perpendicular to the fibril axis is more ifor Aβ than for hIAPP; however, the standard deviation (sd) in $E_{P, hIAPP}$ is higher than $E_{P, A\beta}$. This sd indicates that the number of different conformations contributing to the proton conduction is higher during the aggregation of hIAPP than Aβ.

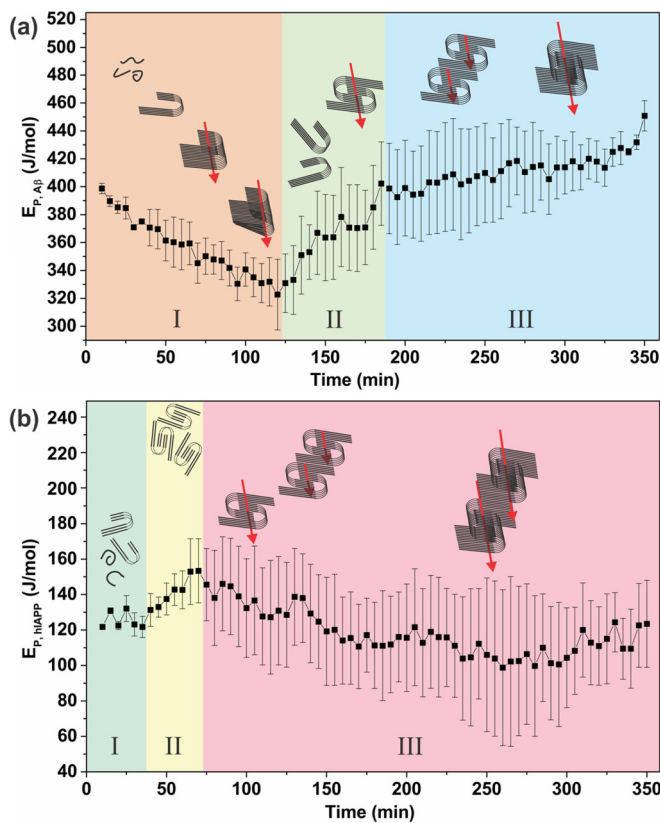


FIG. 5. The modulus of activation energy of proton conduction with mean±sd (calculated from four to five independent experiments using fresh samples) for (a) Aβ (1–42) and (b) hIAPP (1–37) with respect to time, shown with the schematic representations of the conformations formed during the aggregation pathway. Regions I, II, and III represent different phases of aggregation for the proteins from the structural perspective.

The aggregation kinetics of these peptides, particularly Aβ, is well explored [38–40]. These studies report two phase aggregation kinetics for Aβ [41]. The two phases were the lag phase and the rapid elongation of nucleation sites to matured fibrils. The kinetics aggregation data for Aβ and hIAPP have the sigmoidal appearance and follow nucleation-dependent polymerization. By performing the experiments on replicates, it was statistically shown that Aβ aggregation follows a sequence of events and occurs by a two-phase process [41]. In the present study, the E_P parameter reflects the growth of the fibril from the perspective of the conformations and structures formed during the aggregation. The E_P varies with the pathway of proton conduction due to changes in the secondary structure (α -helix or β -sheet) content and the direction of elongation (perpendicular to or along the fibril axis) of the fibril. On this basis, the E_P graphs for the aggregation of Aβ and hIAPP demonstrate the three stages of kinetics (regions I, II, and III) as shown in Fig. 5. The regions were divided based on the fact that the data in a particular region showed a linear variation with time. These graphs do not follow the sigmoidal

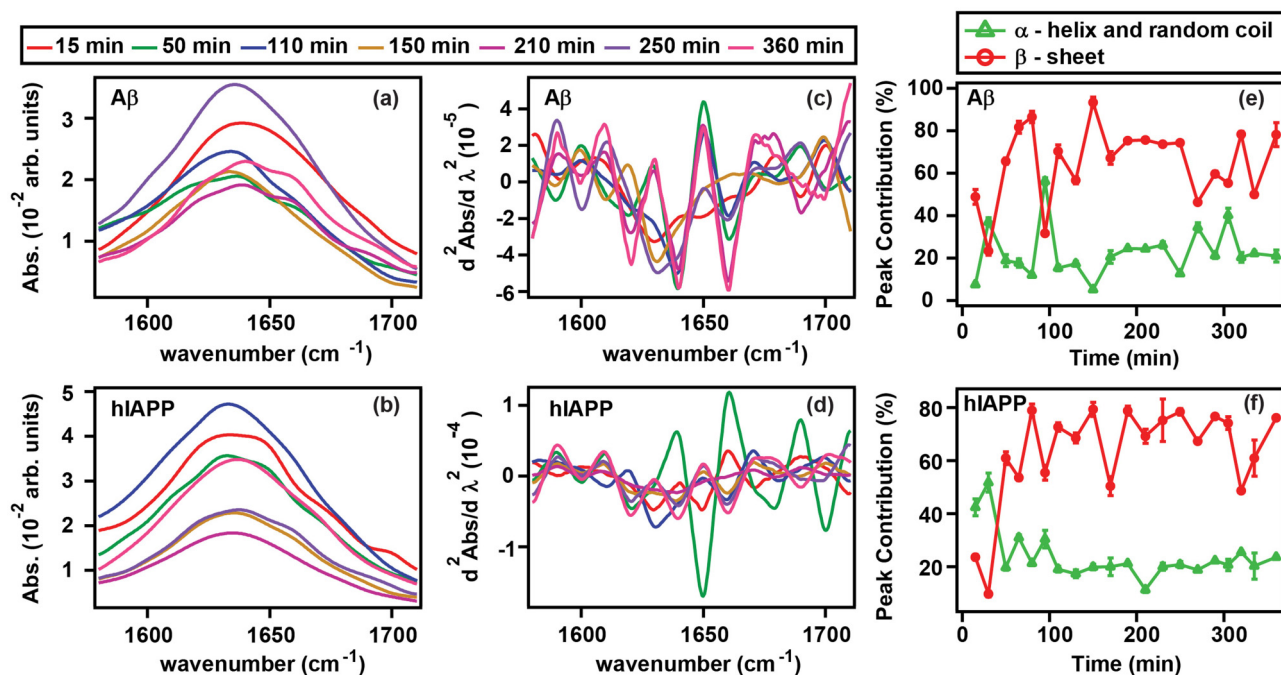


FIG. 6. The FTIR spectra for (a) $A\beta$ and (b) hIAPP. The second derivative of the FTIR spectra is shown in (c) $A\beta$ and (d) hIAPP. The α -helix and β -sheet secondary structure compositions at different times during the experiment for (e) $A\beta$ and (f) hIAPP.

curve, commonly known for protein aggregation, so it is difficult to identify the phases of aggregation kinetics. However, regions I, II, and III in the E_p graphs may possibly include nucleation-elongation phase, fragmentation-elongation phase, and elongation-saturation phase, respectively.

Further, FTIR experiments are carried out to confirm the protein aggregation in the above-mentioned conditions. In total, FTIR spectra at 20 different times were recorded to capture the secondary structure composition of the structures formed during the entire experimental time (360 min). The FTIR spectra and its corresponding second derivatives at 15, 50, 110, 150, 210, 250, and 360 min are shown in Figs. 6(a) and 6(b) and Figs. 6(c) and 6(d), respectively. The FTIR spectra with its second derivatives at rest of the times along with the corresponding secondary structures, determined by analyzing the FTIR spectra, are demonstrated in the Supplemental Material [23]. The FTIR data reveal a higher percentage of β -sheet (the error bars are the fitting errors) in $A\beta$ compared to hIAPP at the initial stages of aggregation, as shown Fig. 6(e) and 6(f). The percentage of β -sheet increases for both $A\beta$ and hIAPP with time, confirming the aggregation of both the proteins at the temperature gradient of 45–40°C. The percentage of α -helix and random coil fluctuates more in $A\beta$ than hIAPP for the entire duration of the experiment. Moreover, the percentage of stable fibrils with β -sheet (higher in $A\beta$ compared to hIAPP), the antiparallel β -sheet (more significant in $A\beta$ than hIAPP), and parallel β -sheet contents also exhibit significant changes in the intermediate times of the experiment (see Tables S1 and S2 in the Supplemental Material [23]). These changes in the secondary structures of $A\beta$ and hIAPP during aggregation may be responsible for the fluctuation in the activation energy of the proton transfer.

B. Effect of resveratrol on the aggregation of $A\beta$ and hIAPP

Res, a polyphenol, has been used to study the inhibition kinetics of $A\beta$ and hIAPP where Res is shown to inhibit the protein aggregation by stabilizing small oligomers [42–44]. Figures 7(a) and 7(b) are displaying the modulus of E_p for AB1R1 and AB1R5, and for A1R1 and A1R5, respectively. We observed that $E_{p, A\beta+Res}$ for AB1R1 is less compared to the $E_{p, A\beta}$ in the entire duration of the experiment, suggesting that the higher number of polar residues are taking part in the proton transfer in AB1R1 than $A\beta$. The minima of both $E_{p, A\beta+Res}$ and $E_{p, A\beta}$ occur nearly at the same time, indicating an insignificant contribution of Res in AB1R1 aggregation. However, the fall of the $E_{p, A\beta+Res}$ observed until 125 min is nonmonotonous; it first sharply decreases followed by stabilization and finally falls to the minimum value in contrast to the monotonous decrement in the $E_{p, A\beta}$. Moreover, the fluctuations in the $E_{p, A\beta+Res}$ is less compared to that in the $E_{p, A\beta}$. This is attributed to different mechanisms of aggregation for $A\beta$ and AB1R1. The higher sd in $E_{p, A\beta}$ is due to the oligomers having different conformations formed during the rapid aggregation of $A\beta$ whereas in the presence of Res some of the conformations are stabilized, leading to a smaller sd in the $E_{p, A\beta+Res}$. After 125 min, the stabilized oligomers of AB1R1 start binding in such a manner that the number of proton transfer sites is reduced, which is observed as an increment in the $E_{p, A\beta+Res}$. In the case of $A\beta$, the increment in $E_{p, A\beta}$ after 120 min was due to the attachment of oligomers in a perpendicular direction to the fibril axis; however, the growth direction for AB1R1 is difficult to comment on.

In the case of AB1R5, the minima of $E_{p, A\beta+Res}$ fall at 20 min. However, this decrement in the $E_{p, A\beta+Res}$ is smaller than both $E_{p, A\beta}$ for $A\beta$ and $E_{p, A\beta+Res}$ for AB1R1. This is

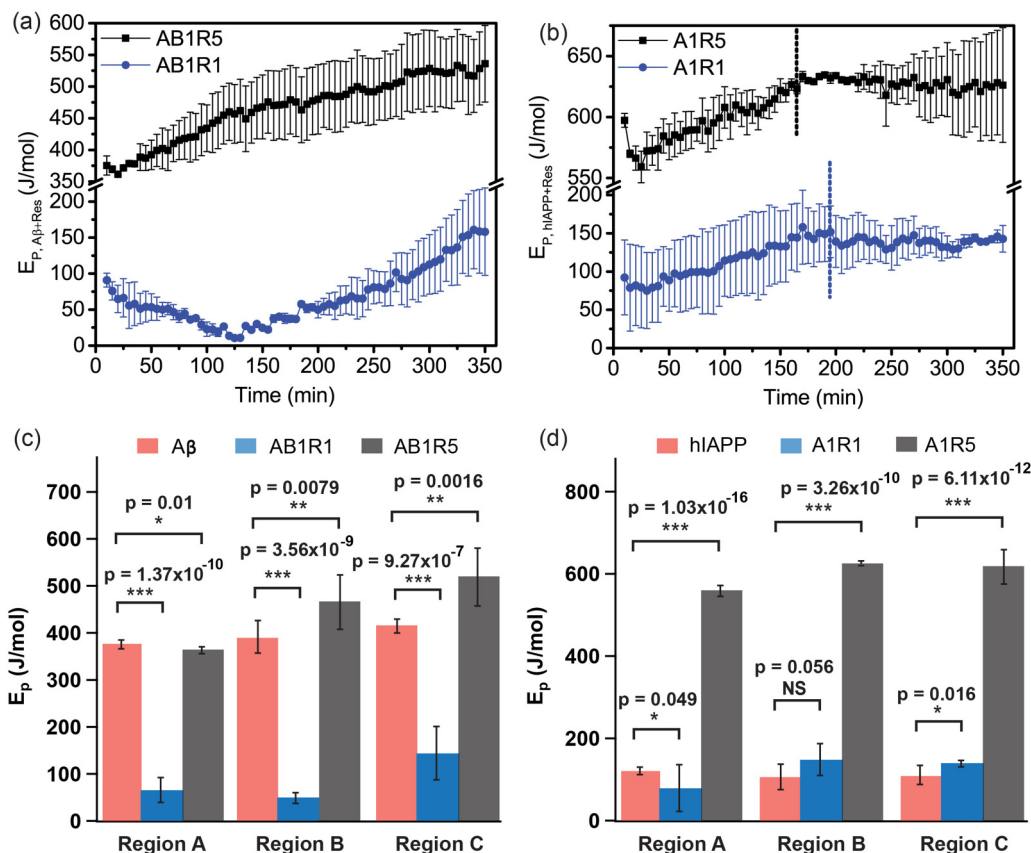


FIG. 7. The modulus of activation energy of proton conduction with mean \pm sd (calculated from four to five independent experiments using fresh samples) in the presence of Res for (a) A β (1–42) and (b) hIAPP (1–37) with time. The statistical comparison between the groups (c) A β -ABIR1 and A β -ABIR5, (d) hIAPP-AIR1, and hIAPP-AIR5. The regions A, B, and C span 15–30, 180–195, and 320–335 min, respectively. Statistical significance was denoted as * $p < 0.05$, ** $p < 0.01$, *** $p < 0.001$, and NS (not significant).

attributed to a more significant inhibitory effect of Res on A β aggregation compared to AB1R1. Through surface-plasmon resonance measurements, it was shown that Res is capable of binding efficiently with both monomers as well as fibrils of A β [45]. We speculate that Res binds to the monomers and nucleation sites at the initial phase of the aggregation and thus does not allow the formation of larger oligomers of AB1R5. Ziao *et al.* reported that Res molecules bind to the *N*-terminus and middle region of the A β protein sequence including few polar residues, and also do not avoid the formation of the oligomers due to no interaction with the *C*-terminus [46]. This suggests that two processes, (i) reduction in the total number of side chains of polar residues due to binding of Res causing increment in the $E_{p, A\beta+Res}$ and (ii) increment in proton wire because of oligomer formation causing decrement in the $E_{p, A\beta+Res}$, occur simultaneously in the initial phase, and both processes result in the overall smaller drop of the $E_{p, A\beta+Res}$ until 20 min. After that, these smaller oligomers of AB1R5 bind with themselves in different conformations, leading to an increase in the $E_{p, A\beta+Res}$. Since the formation of larger oligomers of AB1R5 is inhibited by Res, finally, saturation in the $E_{p, A\beta+Res}$ with large sd is observed.

The molecular dynamics study performed by Lolicato *et al.* [47] revealed that in the molar ratio of 1:1, Res reduces the number of interpeptide contacts in the dimer species of hIAPP. Hence, the number of polar residues contributing to

the proton conduction will reduce, and due to this event, the $E_{p, hIAPP+Res}$ for AIR1 increases. It has also been shown that Res interacts weakly with hIAPP, mainly because the hydrophobic residues in two monomers of hIAPP form a stable pocket that can accommodate a single Res molecule, and hence the second Res molecule has a weak interaction with the peptide. The replica-exchange-based molecular dynamics simulation revealed that the Res reduces the lateral growth of β -sheets [48]. These results indicate that Res inhibits hIAPP aggregation merely through weak interaction, which hinders the formation of larger oligomers of AIR1. The results of these studies are consistent with the observation that the formation of hIAPP oligomers (in the absence of Res) is spanned for 70 min [Fig. 5(b)], which is delayed to 195 min for AIR1. After increase in the $E_{p, hIAPP+Res}$, the proton conduction of the formed oligomers of AIR1 saturates with smaller sd, signifying fewer conformations.

In the case of AIR5, the phase corresponding to the formation of oligomers is up to 165 min and has fewer conformations than AIR1. The inhibitory effect of Res is more pronounced in AIR5, reflected in the earlier saturation of the $E_{p, hIAPP+Res}$ for AIR5. Govindan *et al.* have reported clusters of hIAPP proteins and Res molecules as nanoassembly having hIAPP positioned outside and Res molecule inside of the cluster [49]. In this case for AIR5, the clusters populate with time, leading to greater increase in the activation energy due to

a reduction in the total number of sites responsible for proton hopping. Previously, the Res has been shown to lock the hIAPP helical intermediates through molecular dynamics [47] and experimental [44] studies. As the secondary structures of the intermediates are helical, the proton conduction will be inhibited. This explains the higher E_P , hIAPP+Res for A1R5 in comparison to both A1R1 and hIAPP and the early saturation of E_P , hIAPP+Res.

Further, the groups $A\beta$ -AB1R1, $A\beta$ -AB1R5, hIAPP-A1R1, and hIAPP-A1R5 were statistically compared. The results of unpaired two tail Student's t -test statistical analysis of the groups are shown in Figs. 7(c) and 7(d) for regions A (15–30 min), B (180–195 min), and C (320–335 min). The groups $A\beta$ -AB1R1 and $A\beta$ -AB1R5 are statistically significant in all the regions. Moreover, hIAPP-A1R1 groups also exhibit significance in region A and C, but these groups are not statistically significant in region B. The hIAPP-A1R5 groups demonstrate the statistical significance in all the regions.

V. CONCLUDING REMARKS

In summary, the efficacy of the used impedance spectroscopy technique is demonstrated for capturing the directional growth during the aggregation of two amyloidogenic proteins ($A\beta$ and hIAPP) at micromolar concentrations. The calculated E_P for these proteins reveal different phases of the directional growth, depicted herein with different regions having distinct patterns in the E_P graph for these proteins obtained under the temperature gradient conditions. The standard deviations in the E_P for these proteins were related to different conformations present during the aggregation. This study deciphers the different pathway of aggregation for these two proteins. $A\beta$ exhibits the higher propensity of aggregation than hIAPP. For $A\beta$, the growth along the fibril axis first dominates the aggregation process [region I in Fig. 5(a)],

succeeded by the elongation in the perpendicular direction to the fibril axis [region II in Fig. 5(a)]. In the case of hIAPP, the monomeric states are initially stabilized [region I in Fig. 5(b)], and furthermore the growth of the protofilament is dominantly perpendicular to the fibril axis [region II in Fig. 5(b)]. In region III, for both the proteins [Figs. 5(a) and 5(b)], the elongations along both the directions compete with each other.

Resveratrol has shown to inhibit the aggregation of these two proteins (in different molar ratio) by stabilizing the small oligomers. In the case of AB1R1, the evolution of the E_P followed similar behavior as that of $A\beta$; however, for AB1R5 remarkable changes in the E_P were observed. This shows that resveratrol has a more pronounced inhibitory effect on $A\beta$ aggregation in the molar ratio of 1:5 (AB1R5) than 1:1 (AB1R1). In the case of hIAPP, the saturation in E_P occurs earlier for 1:5 (A1R5) than 1:1 (A1R1) molar ratio due to the formation of helical structures as intermediates. Finally, the groups $A\beta$ -AB1R1, $A\beta$ -AB1R5, hIAPP-A1R1, and hIAPP-A1R5 were statistically compared in three different regions of the activation energy trajectories. All the groups, except hIAPP-A1R1 in region B, were statistically significant in all the regions. This method may be utilized to investigate the changes in the aggregation pathway for protein-ligand complexes in different conditions. The study of interactions between these two proteins through electrical properties will be the subject matter of further investigation.

ACKNOWLEDGMENTS

P.A., A.S., and S.K. are grateful to Ministry of Human Resource Development (MHRD), India, for providing financial assistantship and A.N.G. acknowledges the support from an APL grant from Sponsored Research and Industrial Consultancy (SRIC), IIT Kharagpur. We acknowledge the central research facility of IIT Kharagpur for FTIR measurements.

-
- [1] C. de Grotthus, Sur la décomposition de l'eau et des corps qu'elle tient en dissolution à l'aide de l'électricité galvanique, *Ann. Chim.* **58**, 54 (1806).
- [2] N. Agmon, The Grotthuss mechanism, *Chem. Phys. Lett.* **244**, 456 (1995).
- [3] J. F. Nagle and H. J. Morowitz, Molecular mechanisms for proton transport in membranes, *Proc. Natl. Acad. Sci. USA* **75**, 298 (1978).
- [4] M. E. Girvin, V. K. Rastogi, F. Abildgaard, J. L. Markley, and R. H. Fillingame, Solution structure of the transmembrane H^+ -transporting subunit c of the F_1F_0 ATP synthase, *Biochemistry* **37**, 8817 (1998).
- [5] D. Pogoryelov, Ö. Yildiz, J. D. Faraldo-Gómez, and T. Meier, High-resolution structure of the rotor ring of a proton-dependent ATP synthase, *Nat. Struct. Mol. Biol.* **16**, 1068 (2009).
- [6] J. T. M. Kennis, D. S. Larsen, I. H. M. van Stokkum, M. Vengris, J. J. van Thor, and R. van Grondelle, Uncovering the hidden ground state of green fluorescent protein, *Proc. Natl. Acad. Sci. USA* **101**, 17988 (2004).
- [7] B. Salna, A. Benabbas, J. T. Sage, J. Van Thor, and P. M. Champion, Wide-dynamic-range kinetic investigations of deep proton tunnelling in proteins, *Nat. Chem.* **8**, 874 (2016).
- [8] S. Yoshikawa, K. Muramoto, K. Shinzawa-Itoh, H. Aoyama, T. Tsukihara, K. Shimokata, Y. Katayama, and H. Shimada, Proton pumping mechanism of bovine heart cytochrome c oxidase, *Biochim. Biophys. Acta, Bioenerg.* **1757**, 1110 (2006).
- [9] J. Vilhjálmsdóttir, A.-L. Johansson, and P. Brzezinski, Structural changes and proton transfer in cytochrome c oxidase, *Sci. Rep.* **5**, 12047 (2015).
- [10] S. S. Hasan, E. Yamashita, D. Baniulis, and W. A. Cramer, Quinone-dependent proton transfer pathways in the photosynthetic cytochrome b_6f complex, *Proc. Natl. Acad. Sci. USA* **110**, 4297 (2013).
- [11] K. Murata, Y. Fujii, N. Enomoto, M. Hata, T. Hoshino, and M. Tsuda, A study on the mechanism of the proton transport in bacteriorhodopsin: The importance of the water molecule, *Biophys. J.* **79**, 982 (2000).

- [12] H. Luecke, B. Schobert, H. T. Richter, J. P. Cartailier, and J. K. Lanyi, Structural changes in bacteriorhodopsin at 2 Å resolution, *Science* **286**, 255 (1999).
- [13] R. Nelson, M. R. Sawaya, M. Balbirnie, A. Ø. Madsen, C. Riek, R. Grothe, and D. Eisenberg, Structure of the cross- β spine of amyloid-like fibrils, *Nature (London)* **435**, 773 (2005).
- [14] M. R. Sawaya, S. Sambashivan, R. Nelson, M. I. Ivanova, S. A. Sievers, M. I. Apostol, M. J. Thompson, M. Balbirnie, J. J. W. Wiltzius, H. T. McFarlane, A. Ø. Madsen, C. Riek, and D. Eisenberg, Atomic structures of amyloid cross- β spines reveal varied steric zippers, *Nature (London)* **447**, 453 (2007).
- [15] D. Eisenberg and M. Jucker, The amyloid state of proteins in human diseases, *Cell* **148**, 1188 (2012).
- [16] J. D. Green, C. Goldsbury, J. Kistler, G. J. Cooper, and U. Aebi, Human amylin oligomer growth and fibril elongation define two distinct phases in amyloid formation, *J. Biol. Chem.* **279**, 12206 (2004).
- [17] M. A. Wälti, F. Ravotti, H. Arai, C. G. Glabe, J. S. Wall, A. Böckmann, P. Güntert, B. H. Meier, and R. Riek, Atomic-resolution structure of a disease-relevant A β (1–42) amyloid fibril, *Proc. Natl. Acad. Sci. USA* **113**, E4976 (2016).
- [18] L. J. Young, G. S. Kaminski Schierle, and C. F. Kaminski, Imaging A β (1–42) fibril elongation reveals strongly polarised growth and growth incompetent states, *Phys. Chem. Chem. Phys.* **19**, 27987 (2017).
- [19] R. R. da Silva, S. V. de Lima, H. P. de Oliveira, C. P. de Melo, I. A. Frías, M. D. Oliveira, and C. A. Andrade, Real-time monitoring of amyloid fibrillation by electrical impedance spectroscopy, *Colloids Surf., B* **160**, 724 (2017).
- [20] A. Affanni, A. Corazza, G. Esposito, F. Fogolari, and M. Polano, Protein aggregation measurement through electrical impedance spectroscopy, *J. Phys.: Conf. Ser.* **459**, 012049 (2013).
- [21] A. Kaushik, R. D. Jayant, S. Tiwari, A. Vashist, and M. Nair, Nano-biosensors to detect β -amyloid for Alzheimer's disease management, *Biosens. Bioelectron.* **80**, 273 (2016).
- [22] A. T. Alexandrescu, Amide proton solvent protection in amylin fibrils probed by quenched hydrogen exchange NMR, *PLoS ONE* **8**, e56467 (2013).
- [23] See Supplemental Material at <http://link.aps.org/supplemental/10.1103/PhysRevE.101.062413> for more information about FTIR analysis.
- [24] D. N. Bopege, M. Petrowsky, M. B. Johnson, and R. Frech, Mass and ion transport in ketones and ketone electrolytes: Comparison with acetate systems, *J. Solution Chem.* **42**, 584 (2013).
- [25] H. Ma, Y. Su, and A. Nathan, Cell constant studies of bipolar and tetrapolar electrode systems for impedance measurement, *Sens. Actuators, B* **221**, 1264 (2015).
- [26] N. Amdursky, E. D. Głowacki, and P. Meredith, Macroscale biomolecular electronics and ionics, *Adv. Mater.* **31**, 1802221 (2019).
- [27] E. Guo and D. R. McKenzie, A post-Gurney quantum mechanical perspective on the electrolysis of water: Ion neutralization in solution, *Proc. R. Soc. London, Ser. A* **473**, 20170371 (2017).
- [28] G. Bitan, A. Lomakin, and D. B. Teplow, Amyloid β -protein oligomerization: Prenucleation interactions revealed by photo-induced cross-linking of unmodified proteins, *J. Biol. Chem.* **276**, 35176 (2001).
- [29] S. L. Bernstein, N. F. Dupuis, N. D. Lazo, T. Wyttchenbach, M. M. Condron, G. Bitan, D. B. Teplow, J. E. Shea, B. T. Ruotolo, C. V. Robinson, and M. T. Bowers, Amyloid- β protein oligomerization and the importance of tetramers and dodecamers in the aetiology of Alzheimer's disease, *Nat. Chem.* **1**, 326 (2009).
- [30] A. Kahler, H. Sticht, and A. H. C. Horn, Conformational stability of fibrillar amyloid- β oligomers via protofilament pair formation: A systematic computational study, *PLoS ONE* **8**, e70521 (2013).
- [31] D. S. Eisenberg and M. R. Sawaya, Implications for Alzheimer's disease of an atomic resolution structure of amyloid- β (1–42) fibrils, *Proc. Natl. Acad. Sci. USA* **113**, 9398 (2016).
- [32] S. Khatun, K. Shikha, A. Ganguly, N. Pawar, and A. N. Gupta, Repulsive interaction induces fibril formation and their growth, *Int. J. Biol. Macromol.* **123**, 20 (2019).
- [33] Y. Li, J. Yan, X. Zhang, and K. Huang, Disulfide bonds in amyloidogenesis diseases related proteins, *Proteins: Struct., Funct. Bioinf.* **81**, 1862 (2013).
- [34] S. Luca, W. M. Yau, R. Leapman, and R. Tycko, Peptide conformation and supramolecular organization in amylin fibrils: Constraints from solid-state NMR, *Biochemistry* **46**, 13505 (2007).
- [35] K. Yanagi, M. Ashizaki, H. Yagi, K. Sakurai, Y. H. Lee, and Y. Goto, Hexafluoroisopropanol induces amyloid fibrils of islet amyloid polypeptide by enhancing both hydrophobic and electrostatic interactions, *J. Biol. Chem.* **286**, 23959 (2011).
- [36] M. Bakou, K. Hille, M. Kracklauer, A. Spanopoulou, C. V. Frost, E. Malideli, L. M. Yan, A. Caporale, M. Zacharias, and A. Kapurniotu, Key aromatic/hydrophobic amino acids controlling a cross-amyloid peptide interaction versus amyloid self-assembly, *J. Biol. Chem.* **292**, 14587 (2017).
- [37] D. H. Lopes, A. Meister, A. Gohlke, A. Hauser, A. Blume, and R. Winter, Mechanism of islet amyloid polypeptide fibrillation at lipid interfaces studied by infrared reflection absorption spectroscopy, *Biophys. J.* **93**, 3132 (2007).
- [38] S. J. Bunce, Y. Wang, K. L. Stewart, A. E. Ashcroft, S. E. Radford, C. K. Hall, and A. J. Wilson, Molecular insights into the surface-catalyzed secondary nucleation of amyloid- β_{40} (A β_{40}) by the peptide fragment A β_{16-22} , *Sci. Adv.* **5**, eaav8216 (2019).
- [39] L. Yu, R. Edalji, J. E. Harlan, T. F. Holzman, A. P. Lopez, B. Labkovsky, H. Hillen, S. Barghorn, U. Ebert, P. L. Richardson *et al.*, Structural characterization of a soluble amyloid β -peptide oligomer, *Biochemistry* **48**, 1870 (2009).
- [40] E. Cerf, R. Sarroukh, S. Tamamizu-Kato, L. Breydo, S. Derclaye, Y. F. Dufrière, V. Narayanaswami, E. Goormaghtigh, J.-M. Ruysschaert, and V. Raussens, Antiparallel β -sheet: A signature structure of the oligomeric amyloid β -peptide, *Biochem. J.* **421**, 415 (2009).
- [41] E. Hellstrand, B. Boland, D. M. Walsh, and S. Linse, Amyloid β -protein aggregation produces highly reproducible kinetic data and occurs by a two-phase process, *ACS Chem. Neurosci.* **1**, 13 (2010).
- [42] Y. Feng, X. P. Wang, S. G. Yang, Y. J. Wang, X. Zhang, X. T. Du, X. X. Sun, M. Zhao, L. Huang, and R. T. Liu, Resveratrol

- inhibits β -amyloid oligomeric cytotoxicity but does not prevent oligomer formation, *Neurotoxicology* **30**, 986 (2009).
- [43] Y. Porat, A. Abramowitz, and E. Gazit, Inhibition of amyloid fibril formation by polyphenols: Structural similarity and aromatic interactions as a common inhibition mechanism, *Chem. Biol. Drug Des.* **67**, 27 (2006).
- [44] S. Khatun, A. Singh, D. Mandal, A. Chandra, and A. N. Gupta, Quantification of protein aggregation rates and quenching effects of amylin-inhibitor complexes, *Phys. Chem. Chem. Phys.* **21**, 20083 (2019).
- [45] J.-F. Ge, J.-P. Qiao, C.-C. Qi, C.-W. Wang, and J.-N. Zhou, The binding of resveratrol to monomer and fibril amyloid beta, *Neurochem. Int.* **61**, 1192 (2012).
- [46] Z. Fu, D. Aucoin, M. Ahmed, M. Ziliox, W. E. Van Nostrand, and S. O. Smith, Capping of $A\beta_{42}$ oligomers by small molecule inhibitors, *Biochemistry* **53**, 7893 (2014).
- [47] F. Lolicato, A. Raudino, D. Milardi, and C. La Rosa, Resveratrol interferes with the aggregation of membrane-bound human-IAPP: A molecular dynamics study, *Eur. J. Med. Chem.* **92**, 876 (2015).
- [48] P. Jiang, W. Li, J.-E. Shea, and Y. Mu, Resveratrol inhibits the formation of multiple-layered β -sheet oligomers of the human islet amyloid polypeptide segment 22–27, *Biophys. J.* **100**, 1550 (2011).
- [49] P. Nedumpully-Govindan, A. Kakinen, E. H. Pilkington, T. P. Davis, P. Chun Ke, and F. Ding, Stabilizing off-pathway oligomers by polyphenol nanoassemblies for IAPP aggregation inhibition, *Sci. Rep.* **6**, 19463 (2016).